Chemical Science

ROYAL SOCIETY OF CHEMISTRY

EDGE ARTICLE

View Article Online
View Journal | View Issue



Cite this: *Chem. Sci.*, 2023, **14**, 3610

All publication charges for this article have been paid for by the Royal Society of Chemistry



# $Ti_3C_2T_x$ MXene/carbon nanofiber multifunctional electrode for electrode ionization with antifouling activity†

Jingjing Lei,[a] Fei Yu,[b] Haijiao Xie[c] and Jie Ma *[a]

Scaling, corrosion, and biofouling have enormous economic impacts and potential safety hazards to circulating cooling water systems in industry. Capacitive deionization (CDI) technology, through the rational design and construction of electrodes, is expected to tackle these three problems simultaneously. Here, we report a flexible self-supporting $Ti_3C_2T_x$ MXene/carbon nanofiber film fabricated by electrospinning. It served as a multifunctional CDI electrode with high-performance antifouling and antibacterial activity. One-dimensional (1D) carbon nanofibers bridging two-dimensional (2D) $Ti_3C_2T_x$ nanosheets formed a three-dimensional (3D) interconnected conductive network, which expedited the transport and diffusion kinetics of electrons and ions. Meanwhile, the open-pore framework of carbon nanofibers anchored $Ti_3C_2T_x$, which alleviated self-stacking and enlarged the interlayer space of $Ti_3C_2T_x$ nanosheets, thereby offering more sites for ion storage. The electrical double layer-pseudocapacitance coupled mechanism endowed the prepared $Ti_3C_2T_x$/CNF-14 film with high desalination capacity (73.42 ± 4.57 mg $g^{-1}$ at 60 mA $g^{-1}$), rapid desalination rate (3.57 ± 0.15 mg $g^{-1}$ $min^{-1}$ at 100 mA $g^{-1}$), and longish cycling life, and outperformed other carbon- and MXene-based electrode materials. More importantly, on account of the desirable hydrophilicity, good dispersion, and sufficient exposure of the sharp edges of $Ti_3C_2T_x$ nanosheets, $Ti_3C_2T_x$/CNF-14 concurrently delivered an impressive inactivation efficiency against *Escherichia coli*, reaching 99.89% within 4 h. Our study draws attention to the simultaneous killing of microorganisms through the intrinsic characteristics of well-designed electrode materials. These data could aid application of high-performance multifunctional CDI electrode materials for treatment of circulating cooling water.

Received 19th December 2022
Accepted 26th February 2023

DOI: 10.1039/d2sc06946f

rsc.li/chemical-science

## 1 Introduction

The imbalance between the demand and supply of water resources is becoming increasingly prominent, and water purification has become a research "hotspot". With regard to total water consumption, the proportion of industrial water consumption is 60–80%, of which circulating cooling water accounts for the largest proportion (about 70–80% of industrial water consumption). Circulating cooling water is indispensably and widely used in steel, metallurgy, electric power, petrochemical, and other industrial fields. In a circulating cooling water system, a 300 000 kW condensing unit pumps ~33 000 tons of water per hour. At the same time, fresh water must be replenished and, coupled with evaporation loss, results in an enormous amount of water-resource consumption and sewage discharge. The global action on climate change after 2020 has been arranged in the Paris Agreement.[1] As one of the contractual parties, China has committed to the world to reach a carbon peak in 2030 and achieve carbon neutrality in 2060.[2] Formulation of this "dual-carbon" strategic goal brings forward stricter requirements for highly effective and low-consumptive treatment with circulating cooling water.[3]

In a system for circulating cooling water, ions such as $Ca^{2+}$, $Mg^{2+}$, and $Cl^-$ and microorganisms will inevitably lead to scaling, corrosion, and biofouling problems with an increase in circulation times, thereby seriously threatening the efficiency and safety of production. At present, dosing water-quality stabilizers (including bactericides, scaling inhibitors and corrosion inhibitors) are the first choice for the disposal of circulating cooling water.[4,5] However, the dosed chemical agent is also a burden of operation, and circulating cooling water working with residual chemicals will greatly reduce the efficiency of heat transfer, resulting in higher energy consumption.

[a]*Research Center for Environmental Functional Materials, State Key Laboratory of Pollution Control and Resource Reuse, College of Environmental Science and Engineering, Tongji University, 1239 Siping Road, Shanghai 200092, P. R. China. E-mail: jma@tongji.edu.cn*

[b]*College of Marine Ecology and Environment, Shanghai Ocean University, No. 999, Huchenghuan Road, Shanghai, 201306, P. R. China*

[c]*Hangzhou Yanqu Information Technology Co., Ltd, Y2, 2nd Floor, Building 2, Xixi Legu Creative Pioneering Park, 712 Wen'er West Road, Xihu District, Hangzhou, Zhejiang, 310003, P. R. China*

† Electronic supplementary information (ESI) available. See DOI: https://doi.org/10.1039/d2sc06946f

Moreover, water-quality stabilizers such as amino trimethylene phosphonic acid (ATMP), etidronic acid (HEDP) or methyl benzotriazole (TTA) contain nitrogen or phosphorus, which make sewage eutrophic, and then cause red tides and algal blooms.[6] With regard to methods of membrane filtration, including reverse osmosis,[7] nanofiltration,[8] and electrodialysis,[9,10] the membrane is expensive and readily blocked by microorganisms and corrosion products in water during operation. Hence, the membrane must be cleaned regularly, which leads to huge investment costs. Therefore, given the new requirements, exploring a new method under the background of "dual-carbon" is needed urgently.

Capacitive deionization (CDI), as an emerging electrochemical water-treatment technology, is attractive to researchers in water purification because of its low cost, high energy efficiency, environmental friendliness, and portable implementation. Electrode materials (the core component of CDI technology) play a crucial part in the performance and efficiency of deionization.[11–13] Furthermore, desirable functionalities other than ion removal for CDI, such as degradation of organic compounds,[14,15] antifouling activity, and antibacterial activity,[16] can be endowed through the rational design and construction of electrode materials without adding chemical reagents.[17] Two-dimensional (2D) transition-metal carbide or nitride MXenes remove ions through a pseudocapacitive-based intercalation effect.[18] Thus MXenes have been demonstrated to possess a greater desalination capacity than conventional CDI carbon electrodes based on an electric double layer (EDL) mechanism.[19–23] More importantly, the surface functional groups (–O, –OH, and –F) of MXenes endow them with excellent hydrophilicity, which is favorable for antibacterial activity. Rasool *et al.* showed that, compared with the widely reported antibacterial agent graphene oxide,[24,25] $Ti_3C_2T_x$ MXene exhibited stronger antibacterial activity toward Gram-negative *Escherichia coli* and Gram-positive *Bacillus subtilis*.[26] Other attractive properties of MXenes also favor CDI, such as excellent electrical conductivity, mechanical flexibility, chemical stability, and thermal stability. These admirable properties rarely coexist in one kind of material, making MXenes promising high-performance CDI electrodes for efficient treatment of circulating cooling water.[27–29] Unfortunately, due to van der Waals forces, 2D MXene nanosheets tend to self-accumulate and cause irreversible agglomeration, resulting in a serious reduction of exposed active sites, clogging of ion-transport channels and, ultimately, deterioration of the advantageous characteristics stated above.[30] Furthermore, the lack of interconnectivity between nanosheets and a macroscopic powder state hampers the formation of conductive networks and flexible reuse of collections.[31,32] Thus, the construction of multifunctional CDI electrodes formed by flexible and binder-free MXene-based materials with well-designed structures and fully implemented properties remains a great challenge.

Herein, we fabricated the $Ti_3C_2T_x$ MXene/carbon nanofiber electrode with antibacterial and antifouling functions for treatment of circulating cooling water. Electrospinning technology decentralizes MXene nanosheets, and endows multifunctional electrodes with a self-supporting ability. Research on the structure of MXene-based carbon nanofibers has been limited to capacitors and $Li^+/Na^+$ batteries,[33–37] whereas the fascinating properties of ion removal and antibacterial performance in aqueous solution have yet to be investigated. This work is interesting because it exemplifies the rational design of multifunction CDI electrodes. In terms of the dominant function, it manipulates the synergistic cooperation of the EDL mechanism of carbon nanofibers and the pseudocapacitive effect of MXene for efficient desalination. Moreover, it pays unprecedented attention to the intrinsic antimicrobial activity of CDI electrode materials, providing new inspiration to the selection, design, and application of more abundant CDI electrode materials. This work shows that advanced CDI film electrodes with superior mechanical flexibility, anti-biofouling property, and desalination performance can facilitate the broad application prospects of CDI in the treatment of circulating water.

## 2 Results and discussion

A schematic diagram for the fabrication of a $Ti_3C_2T_x$/CNF nanofiber composite film is shown in Fig. 1a. The MAX phase ($Ti_3AlC_2$) was first etched by LiF and HCl to obtain $Ti_3C_2T_x$, which exhibited a typical "accordion-like" feature (Fig. 1b). Etched $Ti_3C_2T_x$ was subjected to ultrasonic exfoliation, which resulted in a few-layer or single-layer structure and a clear 2D sheet-like feature (Fig. 1c). For further dispersion and size reduction, $Ti_3C_2T_x$ was suspended in DMF and then cell-ground ultrasonically in an ice bath to obtain $Ti_3C_2T_x$ nanosheets. PAN was added to the DMF suspension of $Ti_3C_2T_x$ nanosheets for electrospinning, during which $Ti_3C_2T_x$ nanosheets were anchored between PAN frameworks (Fig. 1d). After carbonization, the backbone of the PAN polymer was transformed into carbon nanofibers, and a $Ti_3C_2T_x$/CNF nanofiber composite film was formed. Elemental mapping indicated evenly distributed C, O, Ti, and F on or in the fibers (Fig. 1e), thereby showing the successful coupling of $Ti_3C_2T_x$ nanosheets and carbon nanofibers, and $Ti_3C_2T_x$ nanosheets completed the conversion of 2D to 1D.

As shown in Fig. 2a, the pure PAN nanofiber film was white, but became dark gradually with an increase in $Ti_3C_2T_x$ content. The uniform color indicated good dispersion of $Ti_3C_2T_x$ on the nanofibers macroscopically. Pure PAN nanofibers exhibited a smooth surface and the average diameter was around 300–400 nm, whereas the surface became rough and the fiber diameter increased gradually upon $Ti_3C_2T_x$ addition, with the appearance of characteristic wrinkles (Fig. 2b–g). From the perspective of the relative position of $Ti_3C_2T_x$ and PAN, the $Ti_3C_2T_x$ nanosheets were dispersed by PAN with longitudinal stretching or wrapping through electrospinning, and without obvious agglomeration. These wrinkles arose from the exposed sharp edges of $Ti_3C_2T_x$ nanosheets, which means an increase in the active area for reactions, thereby benefiting the storage of charge and ions as well as antibacterial activity. In addition, the cross-section of the $Ti_3C_2T_x$-added film maintained the state of stacked fibers similar to the PAN fiber film (Fig. S1†), which guarantees fiber toughness and an electron-transport network.

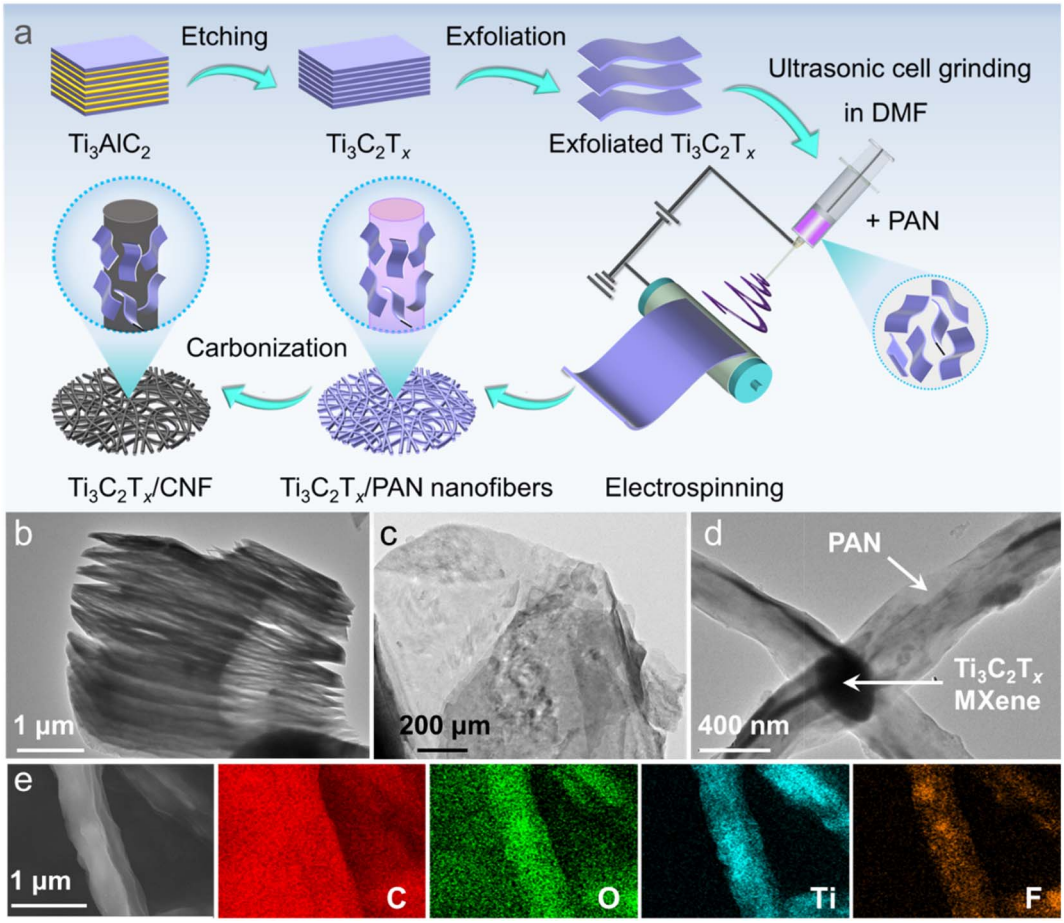


Fig. 1 (a) $Ti_3C_2T_x$/CNF fabrication (schematic). TEM images of etched $Ti_3C_2T_x$ (b), exfoliated $Ti_3C_2T_x$ (c), and $Ti_3C_2T_x$/PAN (d). (e) SEM images of $Ti_3C_2T_x$/PAN and corresponding elemental mappings.

Superior hydrophilicity is essential for the effective application of materials for desalination and sterilization in aqueous solutions, which means higher accessibility. The wettability of all nanofiber films was investigated by measurement of the water contact angle (Fig. 2h). CNF derived from pure PAN is hydrophobic, and the water contact angle decreased slightly from CNF to $Ti_3C_2T_x$/CNF-10, whereas $Ti_3C_2T_x$/CNF-14 presented a wetted state. These data indicated that $Ti_3C_2T_x$/CNF-14 had high hydrophilicity and the greatest possibility of contact with salt ions and bacteria in water, thereby removing them efficiently. This feature may originate from very exposed $Ti_3C_2T_x$ nanosheets with a mass of hydrophilic functional groups (–OH, –F, –O) on the surface, which helped to improve the wettability of composite films.

Stabilization is the most critical step in the conversion of PAN to CNF, which has a decisive impact on the quality of the final fiber. At this stage, PAN undergoes –CN cyclization, dehydrogenation, and oxidation reactions, so the linear PAN molecule transforms into a stable ladder structure.[38] After stabilization, the thermal stability of fibers is greatly improved, so that they can be infusible and incombustible in the subsequent carbonization process, and the final product CNF maintains the fiber morphology. However, during the stabilization process, the fiber structure and morphology undergo a dramatic transformation, which is prone to defects, and mechanical properties (*e.g.*, toughness and strength) are seriously reduced. $Ti_3C_2T_x$ MXene has been reported to be an inorganic filler with high stiffness.[39] After embedding in polymer matrices, it can enhance the mechanical properties of composites greatly. Therefore, in this work, $Ti_3C_2T_x$ with a 2D lamellar structure connected the readily fractured 1D fibers, playing the part of a strong rebar to assist PAN nanofibers (concrete) to resist the structural collapse that is prone to occur during stabilization. Pure PAN-derived CNF had weak mechanical properties and fell into small pieces after deformation (Fig. S2†), thereby making it difficult to prepare self-supporting films.[40] The flexibility and mechanical properties of the fiber films were proportional to the content of $Ti_3C_2T_x$. The obtained $Ti_3C_2T_x$/CNF-14 performed the best, which was attested by various mechanical deformations, such as bending, rolling, and twisting (Fig. 2i).

Thermogravimetric analysis (TGA) was undertaken on all samples (Fig. 2j). The mass loss of bulk $Ti_3C_2T_x$ at 150 °C was 8.39%, which could be ascribed to the evaporation of the remaining DMF and removal of the water in the $Ti_3C_2T_x$ interlayer and functional groups on the $Ti_3C_2T_x$ surface.[33,41] The mass loss of the pure PAN film at 1000 °C was 54.59%. Based on

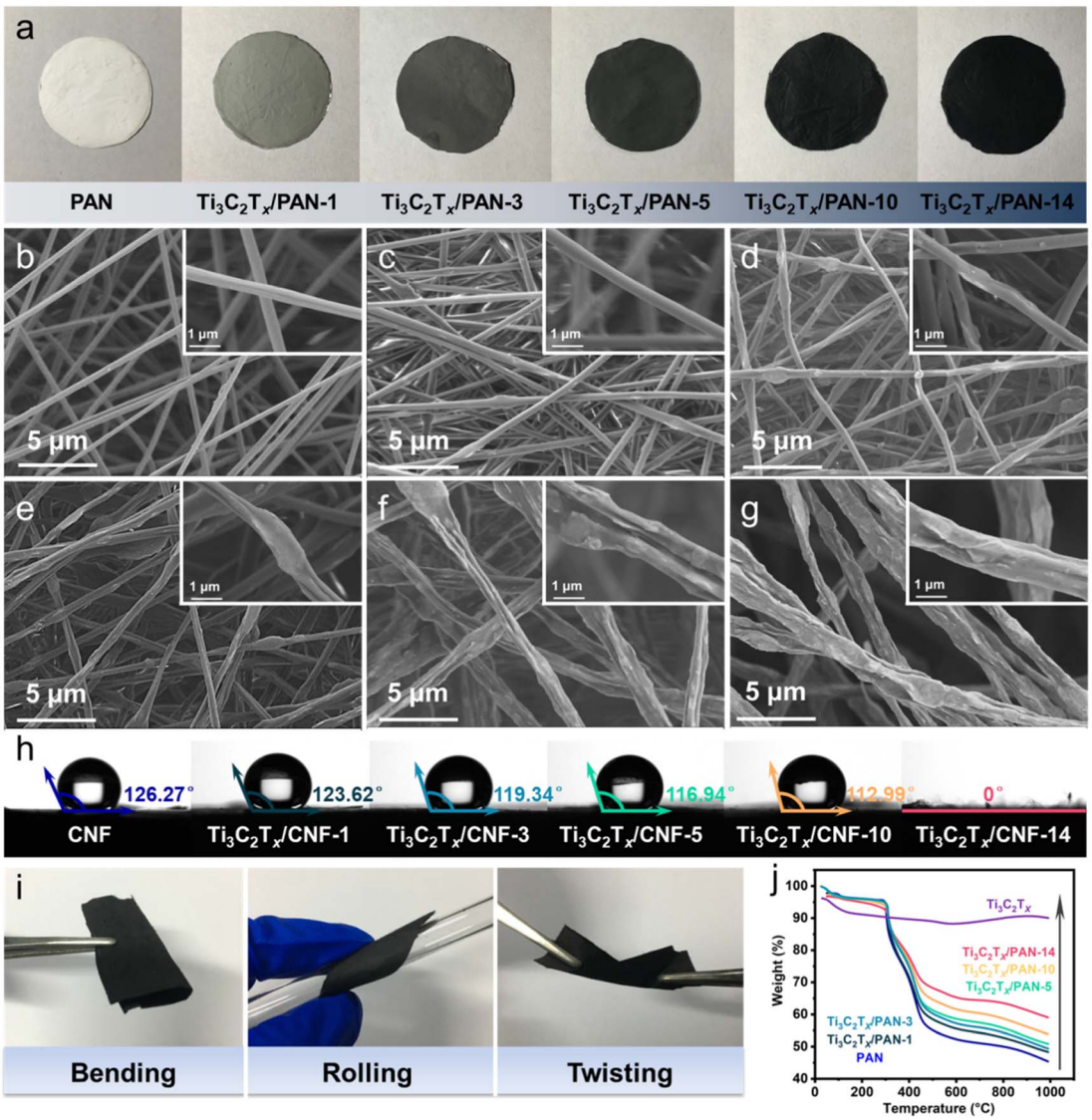


Fig. 2 (a) Optical images of a disk (diameter = 25 mm) cut from as-spun nanofiber films with different $Ti_3C_2T_x$ concentrations. SEM images of a PAN nanofiber film (b), $Ti_3C_2T_x$/PAN-1 (c), $Ti_3C_2T_x$/PAN-3 (d), $Ti_3C_2T_x$/PAN-5 (e), $Ti_3C_2T_x$/PAN-10 (f), and $Ti_3C_2T_x$/PAN-14 (g). Optical images of the water contact angle (h) and the flexibility of $Ti_3C_2T_x$/CNF-14 (i); (j) TGA curves of as-spun nanofiber films with different $Ti_3C_2T_x$ concentrations.

the total weight loss percentage of composite films *versus* the pure PAN film at the same temperature (1000 °C), the mass loading of $Ti_3C_2T_x$ in composite films was estimated and summarized in Table S1.† According to the calculations, a composite film composed of 6.1 wt% $Ti_3C_2T_x$ could be fabricated with only 1 wt% $Ti_3C_2T_x$ addition to the electrospinning solution, whereas the $Ti_3C_2T_x$ mass loading in $Ti_3C_2T_x$/CNF-14 was 23.09%.

In the XRD pattern (Fig. 3a), the diffraction peak at 2 $\theta$ = 16.42° was attributed to the (100) crystal plane of PAN fibers. A strong diffraction peak at 6.44° appeared when $Ti_3C_2T_x$ was doped, which could be attributed to the characteristic diffraction peak of the $Ti_3C_2T_x$ (002) crystal plane.[42] As the $Ti_3C_2T_x$ content increased, the peak shifted from 6.44° to the left to 5.88°, which corresponded to enlargement of the interlayer space of $Ti_3C_2T_x$.[43] This phenomenon was due to the good dispersion between PAN and $Ti_3C_2T_x$, which is favorable for the insertion and deintercalation of ions. In the FTIR spectra (Fig. 3b), the absorption peaks in the range 1500–1600 $cm^{-1}$ were C=C and C=N stretching vibrations belonging to CNF. A peak bulge at 1670 $cm^{-1}$ was a result of the overlapping frequencies of conjugated C=C and C=N bonds.[34] The absorption peaks around 1454 $cm^{-1}$ and 1210 $cm^{-1}$ represented the in-plane bending vibrations of C–H of CNF. The absorption peaks of the O–H stretching vibration of the $Ti_3C_2T_x$ surface group were at 3630–3740 $cm^{-1}$, whereas the peaks at 500–530 $cm^{-1}$ indicated the existence of the Ti–C bonds of $Ti_3C_2T_x$. The Raman spectra in Fig. 3c show the in-plane ($E_g$) and out-of-plane ($A_{1g}$) vibration modes for the C atoms of $Ti_3C_2T_x$ to be around 640 $cm^{-1}$, whereas the peak at 435 $cm^{-1}$

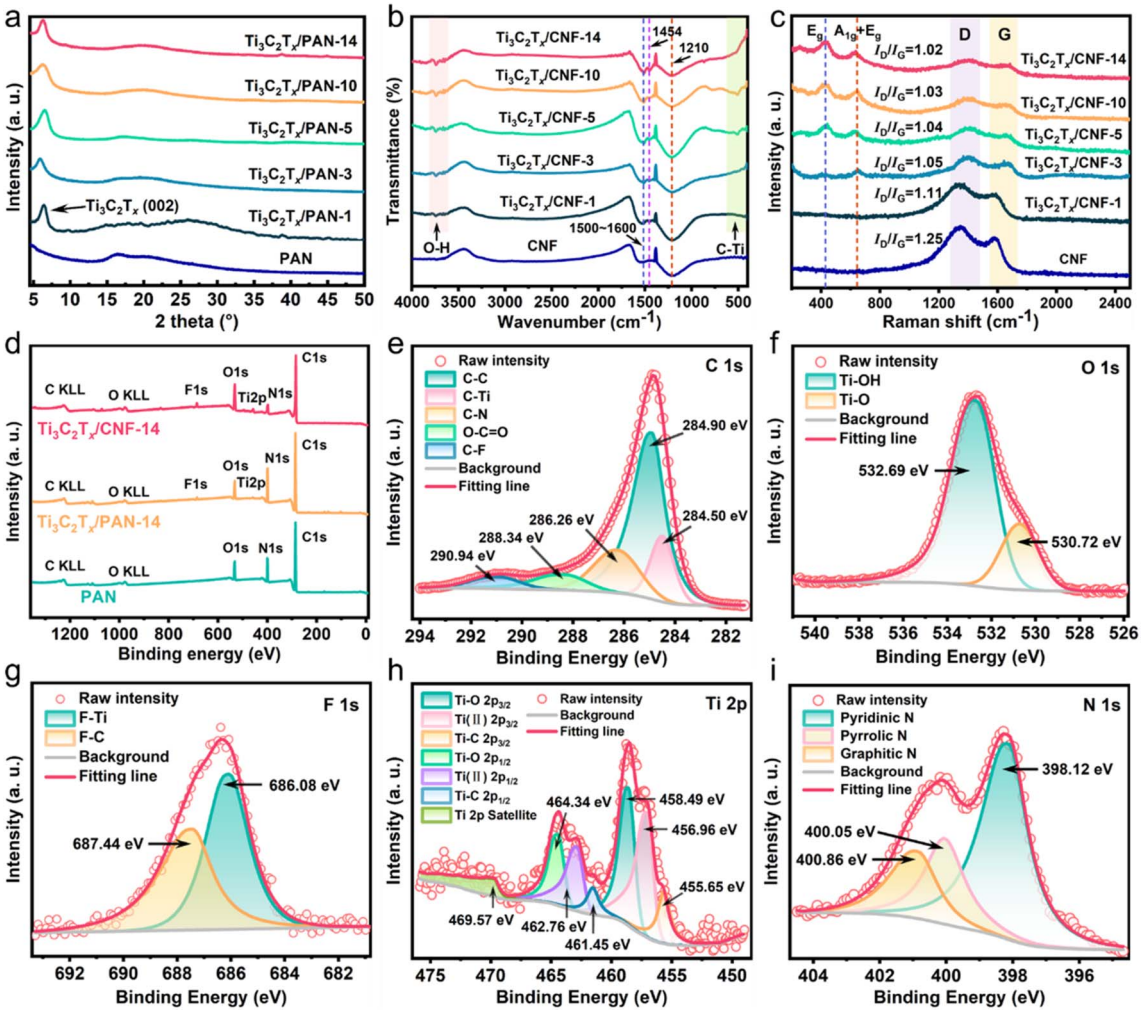


Fig. 3 XRD patterns (a), FTIR data (b), and Raman spectra (c) of samples. (d) XPS surface survey scan spectra of $Ti_3C_2T_x$/CNF-14, $Ti_3C_2T_x$/PAN-14, and PAN. High-resolution XPS spectra of C 1s (e), O 1s (f), N 1s (g), F 1s (h), and Ti 2p (i) of $Ti_3C_2T_x$/CNF-14.

was assigned to the $E_g$-group vibration originating from in-plane Ti atoms.[37] The broad peaks at 1330–1400 $cm^{-1}$ and 1587–1683 $cm^{-1}$ corresponded to the defect-induced mode (D-band) and graphite-induced mode (G-band), respectively. The D-band denoted the $sp^3$ hybrid-disordered carbon structure, whereas the G-band represented the $sp^2$ hybrid graphitic carbon structure. A small intensity ratio of the D-band and G-band ($I_D$/$I_G$) signifies higher graphitization.[44] The value of $I_D/I_G$ decreased from 1.25 to 1.02 as the $Ti_3C_2T_x$ content increased, signifying that $Ti_3C_2T_x$ contributed to transformation of the internal structure of fibers to the graphitic carbon structure during carbonization, which is conducive to the transport of electrons for CDI.

Fig. 3d shows that CNF was composed of C, O, and N elements. Ti and F elements in $Ti_3C_2T_x$/PAN-14 and $Ti_3C_2T_x$/CNF-14 were evidence for the existence of $Ti_3C_2T_x$. In the C 1s spectra of $Ti_3C_2T_x$/CNF-14 (Fig. 3e), the peaks at 284.50, 284.90, 286.26, 288.34, and 290.94 eV could be assigned to C–C, C–Ti, C–N, O–C=O, and C=F bonds, respectively. The O 1s spectra in Fig. 3f could be decoupled into Ti–O (530.72 eV) and Ti–OH (532.69 eV). For F 1s spectra (Fig. 3g), the peaks centered at 686.08 and 687.44 eV correspond to the F–Ti and F–C bonds, respectively. The data stated above confirmed the abundant functional groups (–F, –OH and –O) on the $Ti_3C_2T_x$ surface. The Ti 2p XPS spectra of $Ti_3C_2T_x$/CNF-14 (Fig. 3h) could be deconvolved into three doublets and one satellite peak (469.57 eV). The peaks at 455.65 and 462.76 eV could be allotted to the most predominant Ti–C $2p_{3/2}$ and Ti–C $2p_{1/2}$ in $Ti_3C_2T_x$, whereas the other two doublets were Ti–O $2p_{3/2}$ (458.49 eV), Ti–O $2p_{1/2}$ (464.34 eV), Ti(II) $2p_{3/2}$ (456.96 eV), and Ti(II) $2p_{1/2}$ (462.76 eV),[45] which are analogous to those of bulk $Ti_3C_2T_x$.[46] Furthermore, in the deconvoluted N 1s spectra (Fig. 3i), the peaks located at 398.12, 400.05, and 400.86 eV supported the presence of pyridine-N, pyrrolic-N, and graphitic-N, respectively. Diverse N heteroatoms are favorable for CDI.[47] Graphite-N can improve the electronic conductivity of a carbon framework. Edge-type nitrogen configurations (pyridine-N and pyrrole-N) are beneficial to the wettability of the carbon structure thus improving the accessibility of the salt solution, and can also enhance the redox reaction thus conducive to pseudocapacitance.[48] Overall,

a heteroatomic N atom is more electronegative than a C atom, which induces charge redistribution, resulting in a higher electron density, thereby increasing the ability to attract cations/anions.

As shown in Fig. 4a and S3a,† all CV curves of CNF and $Ti_3C_2T_x$/CNF-14 had no peaks in the range −0.2 V to 0.6 V, exhibiting an approximately rectangular shape, which indicates that the capacitive response may be mainly due to EDL capacitance rather than electrochemical redox reactions. The CV curves of $Ti_3C_2T_x$/CNF-14 were slightly distorted compared with those of CNF, which is evidence of pseudocapacitance.[49] Furthermore, the distribution of the CV curves was very symmetrical, reflecting that the salt ions could be reversibly and efficiently adsorbed to and desorbed from the electrode. Notably, $Ti_3C_2T_x$/CNF-14 possessed a higher specific capacitance than that of CNF because the area of the CV curve was larger (Fig. 4b). Moreover, the specific capacitance calculated based on the CV curves of $Ti_3C_2T_x$/CNF-14 was always higher than that of CNF at any scan rate (Fig. S4†). The absence of a platform on GCD profiles in Fig. 4c and S3b† suggests no redox processes. The charge and discharge time of $Ti_3C_2T_x$/CNF-14 was significantly longer than that of CNF (Fig. 4d), which further attests to the larger charge capacity provided by $Ti_3C_2T_x$/CNF-14. This superior capacitive performance was derived from the addition of pseudocapacitive $Ti_3C_2T_x$ and the formation of a unique and rational hierarchical structure. In the EIS study, the Nyquist plots of CNF and $Ti_3C_2T_x$/CNF-14 consisted of a small semicircle and steep linearity (Fig. 4e). According to the fitting results of the equivalent circuit (inset in Fig. 4e), $Ti_3C_2T_x$/CNF-14 had lower internal resistance $R_\Omega$ (1.31 Ω) and charge-transfer resistance $R_{ct}$ (1.02 Ω) than those of CNF ($R_\Omega$ = 2.55 Ω, $R_{ct}$ = 5.04 Ω). These data indicated that $Ti_3C_2T_x$/CNF-14 had better electronic conductivity, which was benefited from the elaborate conductive network of $Ti_3C_2T_x$/CNF-14 formed by 1D CNF bridging 2D $Ti_3C_2T_x$. $Z'$ and $\omega^{-1/2}$ in the low-frequency region were fitted to obtain the Warburg factor. Fig. S5† shows that $Ti_3C_2T_x$/CNF-14 had a smaller slope, suggesting a faster rate of ion diffusion. The GCD long-cycle experiment was undertaken at 2 A $g^{-1}$ to examine the electrochemical stability of $Ti_3C_2T_x$/CNF-14 (Fig. 4f). After 5000 cycles, the charge-and-discharge capacity did not decay, nor did coulombic efficiency or capacity retention. The excellent electrochemical cycle performance of $Ti_3C_2T_x$/CNF-14 could ensure a long service life in CDI applications.

Exploring the antibacterial activity of $Ti_3C_2T_x$/CNF-14 is conducive to the discovery of potential applications in biofouling resistance. Nanomaterials have been reported to be less effective at inactivating Gram-negative bacteria than Gram-positive strains.[24,50] Among them, the representative Gram-negative bacterium *E. coli* has a negatively charged cell wall and cytoplasmic plasma membrane with an isoelectric point of 4–5, which generates many negative charges in the medium. Therefore, *E. coli* is resistant to the negatively charged $Ti_3C_2T_x$. In addition, *E. coli* is covered with a peptidoglycan layer, and protected by an external lipid membrane, which hampers inactivation.[26] Thus, *E. coli* was selected as the target bacterium to determine the antibacterial activity of film samples.

Fig. 5a displays the growth state of *E. coli* on NA after contact with film samples for 4 h. Compared with the control and CNF, the number of colonies upon $Ti_3C_2T_x$ addition declined significantly and was dependent on the $Ti_3C_2T_x$ dose. Therefore, $Ti_3C_2T_x$ was responsible for the antibacterial activity in the composite. Fig. 5b summarizes the results of colony counts in parallel experiments with time intervals. Within 4 h, the colony number in the blank control remained stable, whereas that of CNF decreased slightly, which may have been due to the low

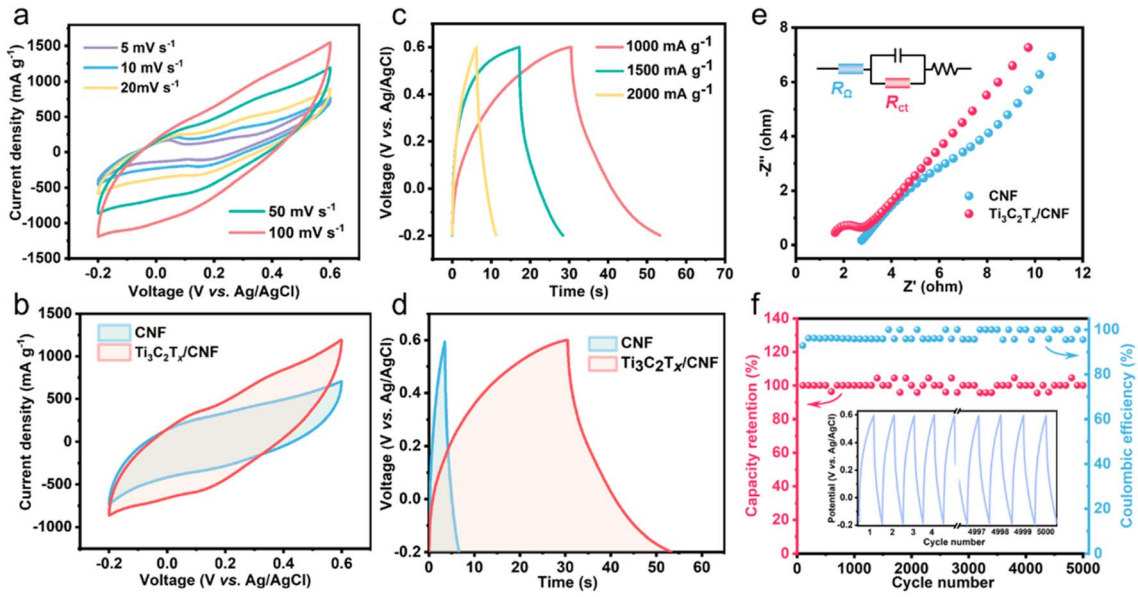


Fig. 4 (a) CV curves of $Ti_3C_2T_x$/CNF-14 at different scan rates. (b) CV curves of CNF and $Ti_3C_2T_x$/CNF-14 at 50 mV $s^{-1}$. (c) GCD profiles of $Ti_3C_2T_x$/CNF-14 at different current densities. (d) GCD profiles of CNF and $Ti_3C_2T_x$/CNF-14 at 1000 mA $g^{-1}$. (e) Nyquist plots of CNF and $Ti_3C_2T_x$/CNF-14. (f) Long-term GCD test of $Ti_3C_2T_x$/CNF-14 at 2 A $g^{-1}$.

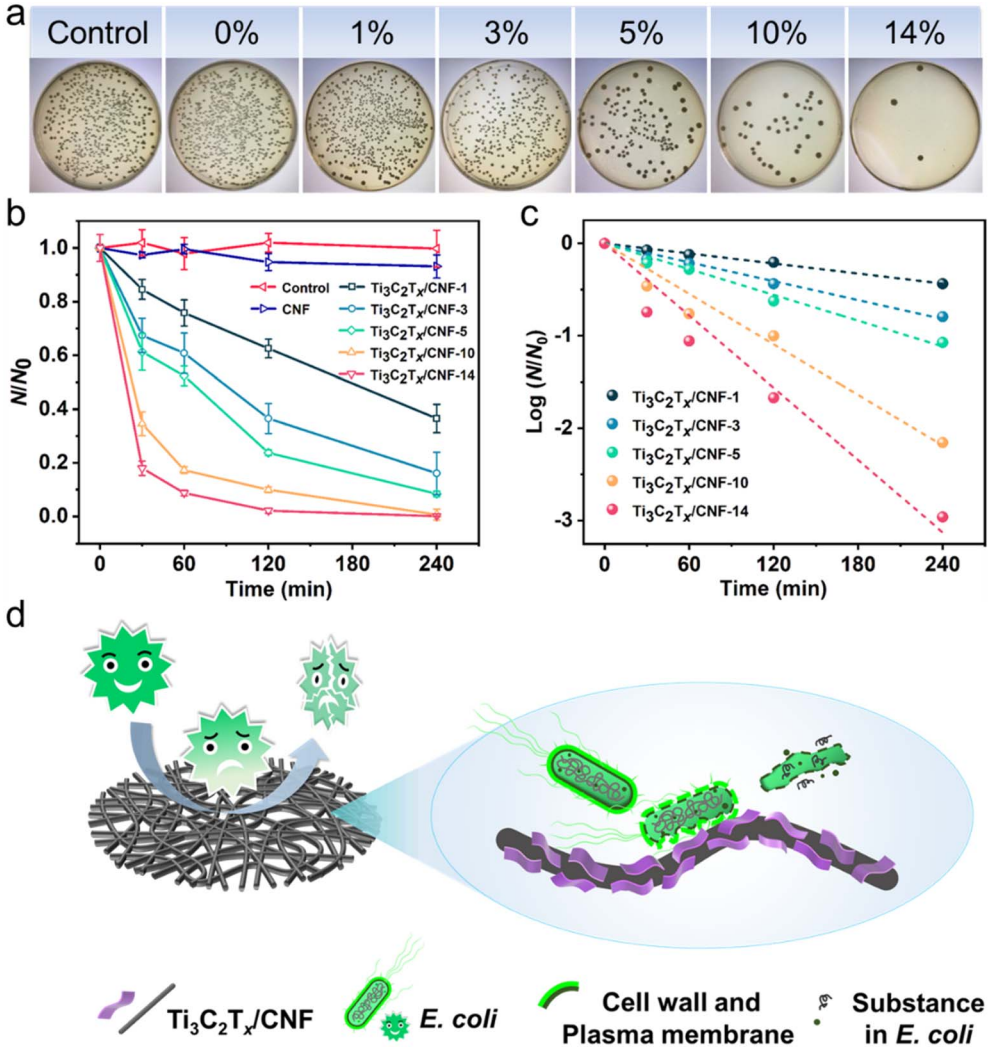


Fig. 5 (a) Photographic images of *Escherichia coli* cultivated on NA plates after treatment with film samples for 4 h (0%, 1%, 3%, 5%, 10%, and 14% refer to the samples CNF, $Ti_3C_2T_x$/CNF-1, $Ti_3C_2T_x$/CNF-3, $Ti_3C_2T_x$/CNF-5, $Ti_3C_2T_x$/CNF-10, and $Ti_3C_2T_x$/CNF-14, respectively). (b) Inactivation effect of all film samples on *E. coli*. *E. coli* suspension in physiological saline water without film samples was used as a control. (c) Linear fitting chart of disinfection kinetics based on Chick's classical disinfection model. (d) Inactivation diagram of $Ti_3C_2T_x$/CNF-14 towards *E. coli* (schematic).

adhesion of nanofibers. The colony number for all $Ti_3C_2T_x$-containing film samples decreased gradually with time, and the inactivation efficiency increased as the amount of $Ti_3C_2T_x$ added increased. $Ti_3C_2T_x$/CNF-14 had conspicuous antibacterial activity, with an inactivation efficiency of 97.86% within 2 h, and reached 99.89% within 4 h. Antibacterial kinetics were explored and are shown in Fig. 5c. The calculated coefficient of determination ($R^2$) and pseudo-first-order rate constant ($k$) according to Chick's classical disinfection model are listed in Table S2,† in which high values of $R^2$ indicate that Chick's model agrees well with experimental data.[51] With an increase in the amount of $Ti_3C_2T_x$ added, the rate of bacterial inactivation increased continuously. The $k$ value increased from 0.00182 $min^{-1}$ for $Ti_3C_2T_x$/CNF-1 to 0.01303 $min^{-1}$ for $Ti_3C_2T_x$/CNF-14, which revealed the exceptional inactivation rate of $Ti_3C_2T_x$/CNF-14.

The physical interaction between sharp edges and the surface of a bacterial membrane plays a vital part in the antibacterial activity of nanosheets.[52,53] The remarkable antibacterial activity of $Ti_3C_2T_x$/CNF-14 was first enhanced by the uniform distribution and high dispersion of $Ti_3C_2T_x$ on CNF, which enabled the sharp edges of $Ti_3C_2T_x$ to be more fully exposed to the *E. coli* suspension. Furthermore, the porous 1D CNF interconnecting and interweaving 2D hydrophilic $Ti_3C_2T_x$ nanosheets made $Ti_3C_2T_x$/CNF-14 highly hydrophilic, which allowed *E. coli* to attach to $Ti_3C_2T_x$/CNF-14 more efficiently, further enhancing the contact between the edges of $Ti_3C_2T_x$ and *E. coli*. Hence, adherent *E. coli* was killed according to direct contact. The inactivation process of $Ti_3C_2T_x$/CNF-14 against *E. coli* is shown in Fig. 5d. Due to favorable hydrophilicity, *E. coli* in the water to be treated can make contact with $Ti_3C_2T_x$/CNF-14 readily. Meanwhile, the sharp edges of $Ti_3C_2T_x$ nanosheets disrupt the plasma membrane and cell wall of *E. coli*, resulting

in cytoplasmic leakage and release of bacterial DNA from the cytosol, which in turn causes the lysis and death of *E. coli* cells.[54] After *E. coli* lysis, $Ti_3C_2T_x$ nanosheets anchored on CNF can continue to sterilize tautologically, so the antibacterial activity of $Ti_3C_2T_x$/CNF-14 has long-lasting stability.

Fig. S6a† illustrates the CDI cell in this study, which was employed in batch mode for the desalination experiment (Fig. S6b†). The indicators for CDI performance of this system in constant-current mode and constant-voltage mode were compared (Fig. S7†). On the premise of close desalination capacity for the two modes, the constant-voltage mode caused a slower desalination rate and greater energy consumption that undesired. Therefore, the constant-current mode was more suitable for our operation system, and can better express the superiority of the electrode configuration. Hence, the constant-current mode was chosen for desalination tests in this work. The indices for the desalination performance of $Ti_3C_2T_x$/CNF-14 capacitive deionization in NaCl solution were studied systematically. First, in NaCl solution (10 mmol), Fig. 6a shows the opposite trends of desalination capacity and desalination rate of $Ti_3C_2T_x$/CNF-14 at 1.2 V: as the current density increased, a desalination capacity of $73.42 \pm 4.57$ mg $g^{-1}$ at 60 mA $g^{-1}$ and a maximum desalination rate of $3.57 \pm 0.15$ mg $g^{-1}$ $min^{-1}$ at 100 mA $g^{-1}$ were reached. In constant-current mode, the desalination rate is determined by the current density, while the cutoff voltage restricts the desalination time of the system. Hence, the desalination capacity of $Ti_3C_2T_x$/CNF-14 increased with an increase in the cutoff voltage, whereas the desalination rate was relatively constant (Fig. 6b). When the initial concentration of NaCl was increased, the desalination capacity of $Ti_3C_2T_x$/CNF-14 increased significantly (Fig. 6c), which was due to more opportunities for contact with ions and the buffering of $Ti_3C_2T_x$ on the co-ion effect. The charge efficiency and energy consumption were calculated for the experiments stated above, and illustrated in Fig. S8a–c,† respectively. Overall, there was a high charge efficiency of $Ti_3C_2T_x$/CNF-14 (around 1), which decreased slightly as the cutoff voltage increased, mainly because the electrode is susceptible to polarization at this time, then undesired side reactions are more likely to occur. The current density does not influence the charge efficiency or energy consumption but, for the cutoff voltage, the increased desalination capacity comes at the expense of a significant increase in energy consumption. Desalination capacity increases with the initial concentration, but energy consumption can be maintained at a low level, as well as a stable desalination rate. Therefore, it can be concluded that $Ti_3C_2T_x$/CNF-14 has great potential for desalination in high-concentration brine. The experiment on seawater desalination was undertaken with two CDI cells connected in series. In NaCl solution with a concentration up to 600 mM, the conductivity of the solution decreased significantly (3429.2 μS $cm^{-1}$) (Fig. S9†), which highlights more possibilities of $Ti_3C_2T_x$/CNF-14 in water purification.

The long-cycle CDI desalination experiments of $Ti_3C_2T_x$/CNF-14 were carried out at 100 mA $g^{-1}$, 1.2 V, and NaCl solution (10 mmol). As shown in Fig. 6d, except for fluctuations in the first 10 cycles, the subsequent desalination capacities remained steady. After 50 cycles, the capacity retention rate was 84.71%, and the adsorption capacity was equal to the desorption capacity, which verified the outstanding cycle and regeneration performance of $Ti_3C_2T_x$/CNF-14. Fig. 6e shows a comparison of the desalination capacity and cycling performance of symmetric CDI cells constructed from $Ti_3C_2T_x$/CNF-14 and CNF, respectively. The desalination capacity of $Ti_3C_2T_x$/CNF-14 was higher than that of CNF at all current densities. Even at a high current density of 100 mA $g^{-1}$, $Ti_3C_2T_x$/CNF-14 retained about 20.08 mg $g^{-1}$ of desalination capacity, which was close to 7-times that of CNF (2.98 mg $g^{-1}$). More importantly, after desalination cycles with different current densities, the desalination capacity of $Ti_3C_2T_x$/CNF-14 could recover to the initial level, which once again demonstrated the superior cycle-regeneration performance and stability of $Ti_3C_2T_x$/CNF-14.

In addition, $Ti_3C_2T_x$/CNF-14 also had outstanding desalination capacity for other common cations in circulating cooling water. Desalination tests were conducted on solutions of $CaCl_2$, $MgCl_2$, and KCl, all at 10 mmol, at 1.2 V (Fig. 6g). The desalination capacities were $23.80 \pm 1.20$ mg $g^{-1}$, $16.95 \pm 2.58$ mg $g^{-1}$, and $23.40 \pm 1.61$ mg $g^{-1}$ within 60 min, respectively. The corresponding molar desalination capacities were $0.21 \pm 0.01$ mmol $g^{-1}$ of $Ca^{2+}$, $0.18 \pm 0.02$ mmol $g^{-1}$ of $Mg^{2+}$, and $0.31 \pm 0.02$ mmol $g^{-1}$ of $K^+$. In particular, the molar desalination capacity of monovalent ions was not approximately twice that of divalent ions, indicating that the desalination behavior of the $Ti_3C_2T_x$/CNF-14 electrode not only originated from the EDL mechanism, but also due to the participation of pseudocapacitance.[55] The CDI performances of the $Ti_3C_2T_x$/CNF-14 electrode for the mixed ion solution containing $CaCl_2$, $MgCl_2$, KCl, and NaCl, all at 10 mmol, and actual circulating cooling water (Table S3†) were tested. Changes in the total dissolved solids (TDS) and conductivity of the solution were monitored, respectively, and are summarized in Fig. 6h. The TDS-removal capacity of $Ti_3C_2T_x$/CNF-14 for the two solutions was 254 mg $L^{-1}$ and 262 mg $L^{-1}$, whereas the corresponding removal efficiency was 34.99% and 16.56%, respectively. The fairly good TDS-removal capacity confirmed the potential ability for $Ti_3C_2T_x$/CNF-14 to cope with actual circulating cooling water with complex components.

Fig. 6i displays the well-designed desalination mechanism of $Ti_3C_2T_x$/CNF-14 capacitive deionization. In the CDI cell in this work, self-supporting $Ti_3C_2T_x$/CNF-14 was used directly as the cathode and anode, without the conventional addition of adhesives and conductive substances that are not contributors to desalination capacity. If the two electrodes are positively and negatively charged, anions and cations will migrate and accumulate in the anode and cathode, respectively. At this time, the interlaced 1D carbon nanofibers act as bridges to connect the dispersed 2D $Ti_3C_2T_x$ sheets. This action leads to formation of a 3D interconnected conductive network that provides fast transport of electrons and ions, whereas the pseudocapacitive ion intercalation-based $Ti_3C_2T_x$ provides an ultra-large interlayer space for ion storage. Therefore, the electric double layer and pseudocapacitance cooperated synergistically and elaborately to facilitate rapid and high-capacity capacitive

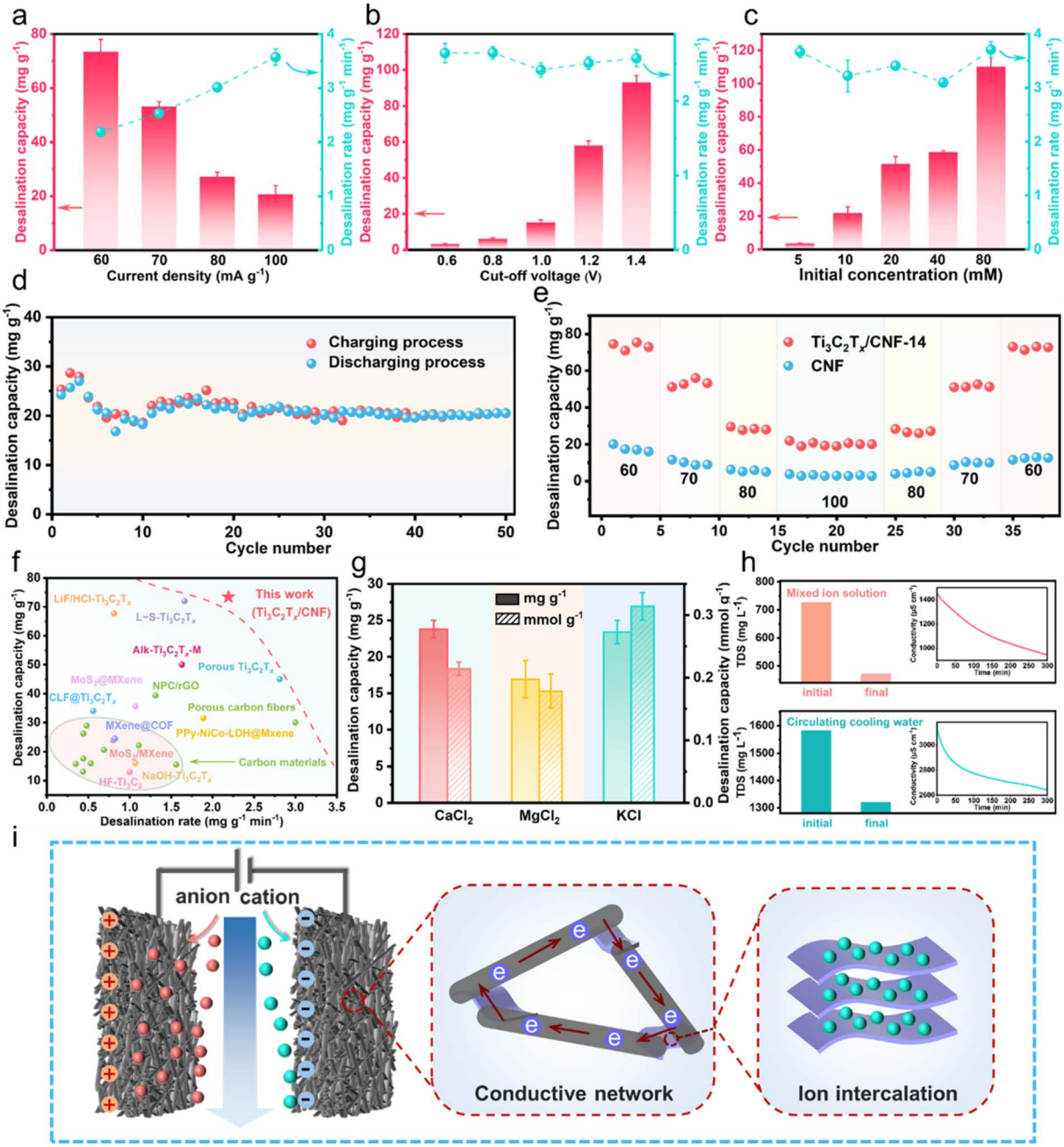


Fig. 6 Capacity and rate of desalination of $Ti_3C_2T_x$/CNF-14 at different current densities (a), cutoff voltages (b), and NaCl initial concentration (c). (d) Cycling and regeneration performance of $Ti_3C_2T_x$/CNF-14 at 100 mA $g^{-1}$ over 50 cycles. (e) Desalination capacity of CNF and $Ti_3C_2T_x$/CNF-14 at different current densities. (f) Comparison of the desalination performance of $Ti_3C_2T_x$/CNF-14 with other carbon- and MXene-based electrode materials. (g) Mass and molar desalination capacity of $Ti_3C_2T_x$/CNF-14 for $CaCl_2$, $MgCl_2$, and KCl. (h) TDS-removal capacity of $Ti_3C_2T_x$/CNF-14 for a mixed ion solution (up) and circulating cooling water (down). Inset shows the change in conductivity. (i) $Ti_3C_2T_x$/CNF-14 capacitive deionization (schematic).

deionization desalination, preceding other carbon- and MXene-based electrode materials (Fig. 6f and Table S4†).

Density functional theory (DFT) calculations were carried out to further explain the ion-storage mechanism (Fig. 7). The structures of Na and Cl adsorbed by CNF, $Ti_3C_2T_x$, and $Ti_3C_2T_x$/CNF were optimized (Fig. S10†). Yellow and blue colors in Fig. 7a indicate electron accumulation and depletion, respectively. These differences in charge density originated from remarkable charge transfer from Na atoms and Cl atoms to the interface of $Ti_3C_2T_x$ and CNF, and a large amount of charge depletion occurred around the adsorbed Na and Cl atoms. The adsorption energies of the three structures for Na and Cl are summarized in Fig. 7c. The adsorption of Na and Cl by CNF was positive (0.45 eV and 0.60 eV), indicating endothermic adsorption,[56] whereas the absolute values were significantly lower than those of $Ti_3C_2T_x$ and the interface. The adsorption energies of

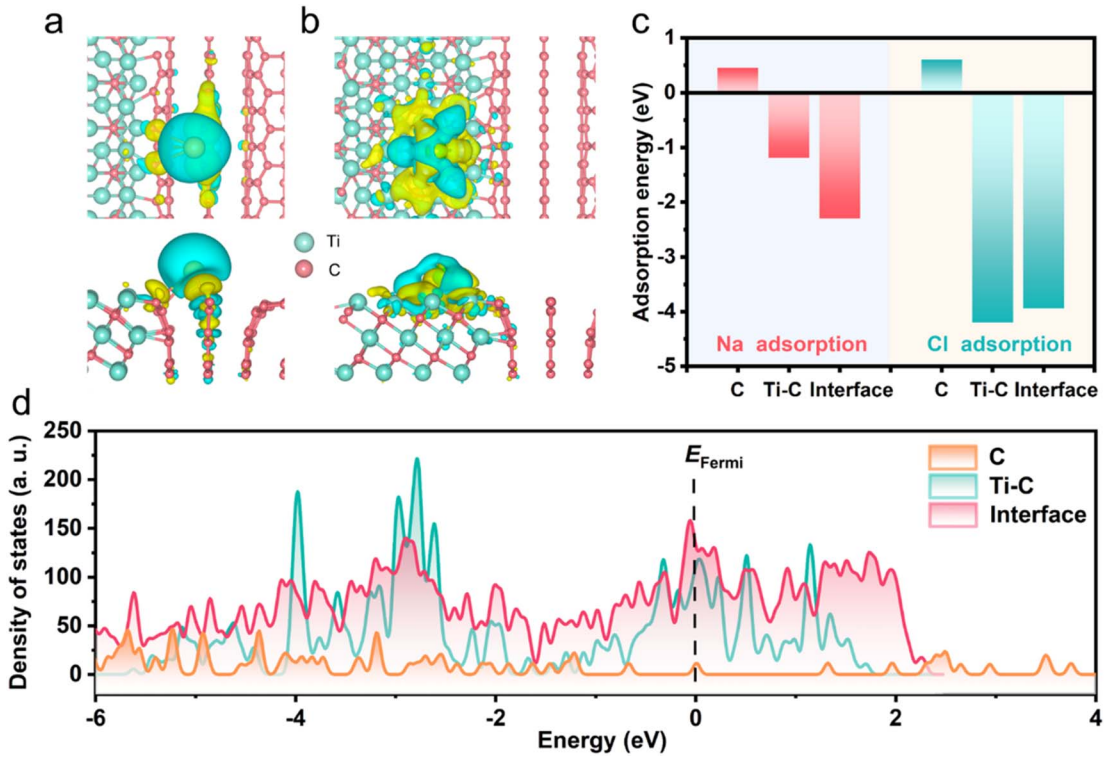


Fig. 7 Differences in charge densities for Na (a) and Cl (b) adsorbed by the interface of CNF and $Ti_3C_2T_x$. (c) Adsorption energy for Na and Cl adsorption of CNF, $Ti_3C_2T_x$, and $Ti_3C_2T_x$/CNF. (d) DOS spectra of CNF, $Ti_3C_2T_x$, and $Ti_3C_2T_x$/CNF.

$Ti_3C_2T_x$ and $Ti_3C_2T_x$/CNF interface for Cl were similar. However, the most negative adsorption energy of the $Ti_3C_2T_x$/CNF interface for Na (−2.30 eV) suggested the strongest adsorption compared with CNF and $Ti_3C_2T_x$ (−1.18 eV). The data stated above may signify that the improved deionization of $Ti_3C_2T_x$/CNF mainly contributed to the enhancement of Na adsorption. Moreover, the density of states (DOS) calculation of the $Ti_3C_2T_x$/CNF interface around the Fermi level (0 eV) in Fig. 7d shows more electron states compared with CNF and $Ti_3C_2T_x$, thereby demonstrating a higher electronic conductivity.[57,58] Analyses of theoretical calculation results showed the superiority of a hierarchical structure constituted by CNF bridging $Ti_3C_2T_x$ in ion diffusion and electron migration, which was consistent with experimental results.

## 3 Conclusions

$Ti_3C_2T_x$ MXene/carbon nanofiber flexible self-supporting film was established for a multifunctional electrode with high-performance capacitive deionization, antifouling, and antibacterial activity. The unique 3D configuration of 1D CNF bridging 2D $Ti_3C_2T_x$ nanosheets endowed $Ti_3C_2T_x$/CNF-14 with ameliorative toughness, hydrophilicity, electrochemical property, and adequate exposure of sharp edges. As the CDI electrode, by synergizing electric double layer mechanism and pseudocapacitive effect, the prepared $Ti_3C_2T_x$/CNF-14 film delivered a high-desalination performance. Moreover, $Ti_3C_2T_x$/CNF-14 showed intriguing antibacterial activity against *E. coli*. This work offers new inspiration for enriching the selection range of CDI electrode materials, and has a positive role in expanding the application of CDI in treatment of circulating cooling water.

## Data availability

The data that support the findings of this study are available from the corresponding author upon reasonable request.

## Author contributions

Jingjing Lei: conceptualization, data curation/analyses, investigation, methodology, validation, visualization, and writing (original draft). Fei Yu: supervision and writing (review and editing). Haijiao Xie: use of software. Jie Ma: funding acquisition, project administration, resources, supervision, and writing (review and editing).

## Conflicts of interest

The authors declare no conflict of interest.

## Acknowledgements

This research was supported by the National Natural Science Foundation of China (22276137) and Fundamental Research Funds for the Central Universities. We are also thankful to the anonymous reviewers for their valuable comments to help to improve this manuscript.

## References

1 M. G. Lawrence and S. Schäfer, Promises and perils of the Paris Agreement, *Science*, 2019, **364**(6443), 829–830.
2 N. Shang, *et al.*, Challenges for large scale applications of rechargeable Zn–air batteries, *J. Mater. Chem. A*, 2022, **10**(31), 16369–16389.
3 J. Zhang, *et al.*, Accurate gas extraction(AGE) under the dual-carbon background: Green low-carbon development pathway and prospect, *J. Cleaner Prod.*, 2022, **377**, 134372.
4 Y. Hu, *et al.*, Characterization of scalants and strategies for scaling mitigation in membrane distillation of alkaline concentrated circulating cooling water, *Desalination*, 2022, **527**, 115534.
5 H.-H. Ou, Q. T. P. Tran and P.-H. Lin, A synergistic effect between gluconate and molybdate on corrosion inhibition of recirculating cooling water systems, *Corros. Sci.*, 2018, **133**, 231–239.
6 X.-Q. Zhang, *et al.*, A partial feed nanofiltration system with stabilizing water quality for treating the sewage discharged from open recirculating cooling water systems, *Sep. Purif. Technol.*, 2020, **234**, 116045.
7 Y. H. Li, *et al.*, Environmental applications of graphene oxide composite membranes, *Chin. Chem. Lett.*, 2022, **33**(12), 5001–5012.
8 R. C. Xiong, X. D. Lei and G. Wei, Controlling pore size and its distribution of gamma-Al2O3 nanofiltration membranes, *Chin. Chem. Lett.*, 2003, **14**(9), 969–972.
9 L. Tian, *et al.*, Degradation of florfenicol in a flow-through electro-Fenton system enhanced by wood-derived block carbon (WBC) cathode, *Chin. Chem. Lett.*, 2022, **33**(11), 4740–4745.
10 Z. N. Wang, *et al.*, Recent advances and trends of heterogeneous electro-Fenton process for wastewater treatment-review, *Chin. Chem. Lett.*, 2022, **33**(2), 653–662.
11 S. Porada, *et al.*, Review on the science and technology of water desalination by capacitive deionization, *Prog. Mater. Sci.*, 2013, **58**(8), 1388–1442.
12 F. Yu, *et al.*, Double-network hydrogel adsorbents for environmental applications, *Chem. Eng. J.*, 2021, **426**, 131900.
13 X. C. Zhang, *et al.*, Industrially-prepared carbon aerogel for excellent fluoride removal by membrane capacitive deionization from brackish groundwaters, *Sep. Purif. Technol.*, 2022, **297**, 121510.
14 M. Ebrahimian Mashhadi, *et al.*, Evaluation of synergistic effects of coupling capacitive deionization (CDI) and UV oxidation processes for saline water treatment, *J. Environ. Chem. Eng.*, 2022, **10**(1), 106909.
15 S. Liang, *et al.*, Integrated ultrafiltration–capacitive-deionization (UCDI) for enhanced antifouling performance and synchronous removal of organic matter and salts, *Sep. Purif. Technol.*, 2019, **226**, 146–153.
16 N. Liu, *et al.*, Simultaneous Efficient Decontamination of Bacteria and Heavy Metals *via* Capacitive Deionization Using Polydopamine/Polyhexamethylene Guanidine Co-deposited Activated Carbon Electrodes, *ACS Appl. Mater. Interfaces*, 2021, **13**(51), 61669–61680.
17 S. Cao, *et al.*, High-Performance Capacitive Deionization and Killing Microorganism in Surface-Water by ZIF-9 Derived Carbon Composites, *Small Methods*, 2021, **5**(12), e2101070.
18 Q. Li, *et al.*, Two-Dimensional MXene-Polymer Heterostructure with Ordered In-Plane Mesochannels for High-Performance Capacitive Deionization, *Angew. Chem., Int. Ed. Engl.*, 2021, **60**(51), 26528–26534.
19 R. L. Zornitta, L. A. M. Ruotolo and L. C. P. M. de Smet, High-Performance Carbon Electrodes Modified with Polyaniline for Stable and Selective Anion Separation, *Sep. Purif. Technol.*, 2022, **290**, 120807.
20 Y. Zhang, *et al.*, MOF-on-MOF nanoarchitectures for selectively functionalized nitrogen-doped carbon-graphitic carbon/carbon nanotubes heterostructure with high capacitive deionization performance, *Nano Energy*, 2022, **97**, 107146.
21 X. Zhang, *et al.*, Industrially-prepared carbon aerogel for excellent fluoride removal by membrane capacitive deionization from brackish groundwaters, *Sep. Purif. Technol.*, 2022, **297**, 121510.
22 Y. Li, *et al.*, Reborn Three-Dimensional Graphene with Ultrahigh Volumetric Desalination Capacity, *Adv. Mater.*, 2021, **33**(48), e2105853.
23 Q. Li, *et al.*, Faradaic Electrodes Open a New Era for Capacitive Deionization, *Adv. Sci.*, 2020, **7**(22), 2002213.
24 M. Wang, *et al.*, Interaction with teichoic acids contributes to highly effective antibacterial activity of graphene oxide on Gram-positive bacteria, *J. Hazard. Mater.*, 2021, **412**, 125333.
25 W. Wei, *et al.*, Distinct antibacterial activity of a vertically aligned graphene coating against Gram-positive and Gram-negative bacteria, *J. Mater. Chem. B*, 2020, **8**(28), 6069–6079.
26 K. Rasool, *et al.*, Antibacterial Activity of Ti(3)C(2)Tx MXene, *ACS Nano*, 2016, **10**(3), 3674–3684.
27 R. Wang, *et al.*, Element-Doped Mxenes: Mechanism, Synthesis, and Applications, *Small*, 2022, **18**(25), e2201740.
28 M. A. Saeed, *et al.*, 2D MXene: A Potential Candidate for Photovoltaic Cells? A Critical Review, *Adv. Sci.*, 2022, **9**(10), e2104743.
29 K. Nasrin, *et al.*, Insights into 2D/2D MXene Heterostructures for Improved Synergy in Structure toward Next-Generation Supercapacitors: A Review, *Adv. Funct. Mater.*, 2022, **32**(18), 2110267.
30 S. Zhang, *et al.*, Heterointerface optimization in a covalent organic framework-on-MXene for high-performance capacitive deionization of oxygenated saline water, *Mater. Horiz.*, 2022, **9**(6), 1708–1716.
31 B. Zhang, A. Boretti and S. Castelletto, Mxene pseudocapacitive electrode material for capacitive deionization, *Chem. Eng. J.*, 2022, **435**, 134959.
32 Y. C. Xiong, F. Yu and J. Ma, Research Progress in Chlorine Ion Removal Electrodes for Desalination by Capacitive Deionization, *Acta Phys.-Chim. Sin.*, 2022, **38**(5), 20–31.
33 A. S. Levitt, *et al.*, Electrospun MXene/carbon nanofibers as supercapacitor electrodes, *J. Mater. Chem. A*, 2019, **7**(1), 269–277.

34 S.-x. Yan, *et al.*, Rational design of hierarchically sulfide and MXene-reinforced porous carbon nanofibers as advanced electrode for high energy density flexible supercapacitors, *Composites, Part B*, 2021, **224**, 109246.
35 Q. Zeng, *et al.*, Sulfur-Bridged Bonds Boost the Conversion Reaction of the Flexible Self-Supporting MnS@MXene@CNF Anode for High-Rate and Long-Life Lithium-Ion Batteries, *ACS Appl. Mater. Interfaces*, 2022, **14**(5), 6958–6966.
36 Y. Guo, *et al.*, MXene-encapsulated hollow Fe3O4 nanochains embedded in N-doped carbon nanofibers with dual electronic pathways as flexible anodes for high-performance Li-ion batteries, *Nanoscale*, 2021, **13**(8), 4624–4633.
37 D. Seo, *et al.*, Hollow $Ti_3C_2$ MXene/Carbon Nanofibers as an Advanced Anode Material for Lithium-Ion Batteries, *ChemElectroChem*, 2021, **9**(1), e202101344.
38 M. S. A. Rahaman, A. F. Ismail and A. Mustafa, A review of heat treatment on polyacrylonitrile fiber, *Polym. Degrad. Stab.*, 2007, **92**(8), 1421–1432.
39 M. Kurtoglu, *et al.*, First principles study of two-dimensional early transition metal carbides, *MRS Commun.*, 2012, **2**(4), 133–137.
40 X. Gong, *et al.*, Enabling a Large Accessible Surface Area of a Pore-Designed Hydrophilic Carbon Nanofiber Fabric for Ultrahigh Capacitive Deionization, *ACS Appl. Mater. Interfaces*, 2020, **12**(44), 49586–49595.
41 Z. Zhou, *et al.*, Layer-by-layer assembly of MXene and carbon nanotubes on electrospun polymer films for flexible energy storage, *Nanoscale*, 2018, **10**(13), 6005–6013.
42 C. Jiang, *et al.*, All-electrospun flexible triboelectric nanogenerator based on metallic MXene nanosheets, *Nano Energy*, 2019, **59**, 268–276.
43 T. Bhatta, *et al.*, High-performance triboelectric nanogenerator based on MXene functionalized polyvinylidene fluoride composite nanofibers, *Nano Energy*, 2021, **81**, 105670.
44 C. Zhang, *et al.*, Boosting Capacitive Deionization Performance of Commercial Carbon Fibers Cloth *via* Structural Regulation Based on Catalytic-Etching Effect, *Energy Environ. Mater.*, 2022.
45 S. Wang, *et al.*, Freestanding Ti3C2Tx MXene/Prussian Blue Analogues Films with Superior Ion Uptake for Efficient Capacitive Deionization by a Dual Pseudocapacitance Effect, *ACS Nano*, 2022, **16**(1), 1239–1249.
46 T. Li, *et al.*, Fluorine-Free Synthesis of High-Purity Ti3C2Tx (T=OH, O) *via* Alkali Treatment, *Angew. Chem., Int. Ed.*, 2018, **57**(21), 6115–6119.
47 A. Amiri, *et al.*, Porous nitrogen-doped MXene-based electrodes for capacitive deionization, *Energy Storage Mater.*, 2020, **25**, 731–739.
48 T. Liu, *et al.*, Exceptional capacitive deionization rate and capacity by block copolymer–based porous carbon fibers, *Sci. Adv.*, 2020, **6**(16), eaaz0906.
49 J. Guo, *et al.*, Graphene-carbon 2D heterostructures with hierarchically-porous P,N-doped layered architecture for capacitive deionization, *Chem. Sci.*, 2021, **12**(30), 10334–10340.
50 S. Shen, *et al.*, Biotransformation of 2D Nanomaterials through Stimulated Bacterial Respiration-Produced Extracellular Reactive Oxygen Species: A Common but Overlooked Process, *Environ. Sci. Technol.*, 2022, **56**(9), 5508–5519.
51 J. Lei, *et al.*, Fabrication of a novel antibacterial TPU nanofiber membrane containing Cu-loaded zeolite and its antibacterial activity toward Escherichia coli, *J. Mater. Sci.*, 2019, **54**(17), 11682–11693.
52 A. Arabi Shamsabadi, *et al.*, Antimicrobial Mode-of-Action of Colloidal Ti3C2Tx MXene Nanosheets, *ACS Sustainable Chem. Eng.*, 2018, **6**(12), 16586–16596.
53 B. Li, *et al.*, Two-dimensional antibacterial materials, *Prog. Mater. Sci.*, 2022, **130**, 100976.
54 O. S. Lee, M. E. Madjet and K. A. Mahmoud, Antibacterial Mechanism of Multifunctional MXene Nanosheets: Domain Formation and Phase Transition in Lipid Bilayer, *Nano Lett.*, 2021, **21**(19), 8510–8517.
55 H. Zhang, *et al.*, Nitrogen, phosphorus co-doped eave-like hierarchical porous carbon for efficient capacitive deionization, *J. Mater. Chem. A*, 2021, **9**(21), 12807–12817.
56 J. Cao, *et al.*, Microbe-Assisted Assembly of Ti(3)C(2)T(x) MXene on Fungi-Derived Nanoribbon Heterostructures for Ultrastable Sodium and Potassium Ion Storage, *ACS Nano*, 2021, **15**(2), 3423–3433.
57 Y. Wang, J. Song and W. Y. Wong, Constructing 2D Sandwich-like MOF/MXene Heterostructures for Durable and Fast Aqueous Zinc-Ion Batteries, *Angew. Chem., Int. Ed. Engl.*, 2022, e202218343.
58 D. Xu, *et al.*, Coupling of bowl-like VS2 nanosheet arrays and carbon nanofiber enables ultrafast Na+-Storage and robust flexibility for sodium-ion hybrid capacitors, *Energy Storage Mater.*, 2020, **28**, 91–100.